



Ultrathin nanoflakes constructed erythrocyte-like Bi_2WO_6 hierarchical architecture *via* anionic self-regulation strategy for improving photocatalytic activity and gas-sensing property

Chunmei Li^a, Gang Chen^{a,*}, Jingxue Sun^{a,*}, Yujie Feng^b, Jijiang Liu^a, Hongjun Dong^{a,c}

^a Department of Chemistry, Harbin Institute of Technology, Harbin 150001, PR China

^b School of Municipal and Environmental Engineering, Harbin Institute of Technology, Harbin 150001, PR China

^c Department of Chemistry, Baicheng Normal University, Baicheng 137000, PR China



ARTICLE INFO

Article history:

Received 23 May 2014

Received in revised form 25 July 2014

Accepted 28 July 2014

Available online 14 August 2014

Keywords:

Anion self-regulation

Erythrocyte-like

Ultrathin nanoflakes

Photocatalytic activity

Gas-sensing property

ABSTRACT

Uniform erythrocyte-like Bi_2WO_6 hierarchical architecture constructed by ultrathin nanoflakes ($\sim 4.4 \text{ nm}$) is firstly obtained *via* an anionic self-regulation strategy without employing any additives at a facile hydrothermal process. The unique hierarchical architecture exhibits high specific surface area and abundant mesoporous distribution, which can provide more reaction active sites and molecule transport channels. The novel structure also facilitates efficiently transfer and separation of charge carriers. In consequence, the photocatalytic activity and gas sensing property are obviously improved relative to the typical Bi_2WO_6 microsphere. This work extends the development of Bi_2WO_6 hierarchical architecture as well as launches a simple, eco-friendly and exemplificative strategy for constructing other Bi-based oxide hierarchical architecture.

© 2014 Elsevier B.V. All rights reserved.

1. Introduction

Environmental problems caused by poisonous wastewater and air pollution have become an arduous challenge to the sustainable development of modern human society. In the last few decades, developing high-efficiency semiconductors photocatalysts [1–3] and gas-sensing materials [4–7] have attracted increasing interest for application to decomposing harmful organic contaminants and detecting hazardous gases effectively. Recently, the dual function semiconductor materials have become the research hotspot due to their unique physicochemical property [8–10]. Among them, three dimensional (3D) hierarchical structures making up of nanoribbons, nanorods, nanosheets etc. are usually considered as potential promising candidates for photocatalysts and gas-sensing materials [11–13], because the assembly of their building units can generate numerous micro-/nano-pores that facilitate molecules diffusion and transport inside them to improve photocatalytic activity and gas-sensing sensitivity. Therefore, designing and constructing of novel semiconductor hierarchical architectures are desired and significant to achieve high-efficiency photocatalysts and gas-sensing materials.

As one of the simplest members of the Aurivillius oxide family, Bi_2WO_6 has received more and more attention because it exhibits excellent intrinsic physical and chemical properties, such as ferroelectric piezoelectricity, pyroelectricity, catalytic behavior, nonlinear dielectric susceptibility and so forth [14–16]. Especially, the 3D Bi_2WO_6 hierarchical structures with specific morphology and high ordered characteristic served as photocatalysts have been studied extensively owing to their important role in the systematic study of structure–property relationships [17–19]. For instance, microsphaeric [20], nest-like [21,22], tyre-/helix-like [23], nanocages-like [24] and clew-like [25] Bi_2WO_6 hierarchical architectures not only exhibit the splendid photocatalytic activity but also display dependencies of activity on the shape, size and structure. Recently, Bi_2WO_6 was successfully applied as gas-sensing material [26,27]. Its high sensitivity, fast response–recovery and good selectivity for ethanol mainly attribute to its curling-like and multilayered hierarchical structure characteristics. Nevertheless, the constructing of these Bi_2WO_6 hierarchical architectures always involves polyvinyl pyrrolidone (PVP), cetyltriethylammonium bromide (CTAB), P123, sodium citrate and colloidal carbon spheres etc. acting as surfactant, template or structure-directing reagent, which may increase complex and difficult production process as well as even cause secondary environment pollution. Therefore, it is necessary for developing a new, simple and eco-friendly technique to achieve the novel Bi_2WO_6 hierarchical architecture to improve

* Corresponding authors. Fax: +86 451 86413753.

E-mail addresses: gchen@hit.edu.cn (G. Chen), jxsun@hit.edu.cn (J. Sun).

its photocatalytic activity, gas-sensing sensitivity and even other physicochemical property.

In this paper, a novel 3D erythrocyte-like Bi_2WO_6 hierarchical architecture assembled by ultrathin nanoflakes with the thickness of ~ 4.4 nm is firstly constructed via an anionic self-regulation strategy without any organic additives at a facile hydrothermal process. The synthesis strategy of erythrocyte-like structure makes the best of structure-directing influence of own WO_4^{2-} anions, which has obviously simplification and pro-environment advantages. Furthermore, the novel 3D architecture shows high specific surface area and abundant mesoporous distribution, which provides more reactive active sites and molecule transport paths. It can also facilitate the transfer and separation of electron–hole pairs. Thus the photocatalytic activity and gas-sensing property compared with the typical Bi_2WO_6 microsphere are distinctly improved. This work may also afford a facile and eco-friendly demonstration strategy for the design and preparation of other high-efficiency bifunctional materials.

2. Experimental

2.1. Preparation and characterizations

All the raw materials were purchased from commercial sources and used without further purification. In a typical synthesis, sodium tungstate ($\text{Na}_2\text{WO}_4 \cdot 2\text{H}_2\text{O}$) was added into the bismuth nitrate ($(\text{Bi}(\text{NO}_3)_3 \cdot 5\text{H}_2\text{O}$) solution drop by drop under vigorous magnetic stirring for 1 h, and then the suspension was transferred into a 25 mL Teflon lined stainless steel autoclave to carry out hydrothermal process at 160°C . After cooling down to room temperature, the solid sample was collected by centrifugation and washed with deionized water and ethanol in turn. Bi_2WO_6 product was finally obtained after drying at 80°C for 20 h. Using the stoichiometric ratio ($\text{W:Bi}=0.5$), the typical hierarchical structured Bi_2WO_6 (B0) microsphere was prepared by 20 h hydrothermal reaction. When the W/Bi ratio was adjusted to 0.9 (80% excess of W source), the erythrocyte-like sample (B80) was prepared by only 3.5 h hydrothermal reaction.

The phase of as-prepared Bi_2WO_6 samples was characterized by powder X-ray diffractometer (XRD, RigakuD/max-2000) equipped with a Cu-K α radiation at a scanning rate of 5° min^{-1} in the 2θ range of $10\text{--}90^\circ$. X-ray photoelectron spectroscopy (XPS) analysis was measured on an American electronics physical HI5700ESCA system with X-ray photoelectron spectrometer using Al K α (1486.6 eV) monochromatic X-ray radiation. The peak positions were corrected against the C 1s peak (284.6 eV) of contaminated carbon. The morphologies of the samples were characterized by field-emission scanning electron microscopy (FESEM, FEI QUANTA 200F). Transmission electron microscopy (TEM) and high-resolution TEM (HR-TEM) of the samples were carried out on FEI Tecnai G2 S-Twin operating at 300 kV. The UV-vis diffuse reflectance spectra (DRS) of the samples were recorded on a UV-vis spectrophotometer (PG, TU-1900) with BaSO_4 as the background between 250 nm and 550 nm at room temperature. The nitrogen adsorption and desorption isotherm, pore size distribution and specific surface area were measured at 77 K using an AUTOSORB-1 Surface Area and Pore Size Analyzer. The photoluminescence (PL) spectra were measured by the Perkin-Elmer LS55 at room temperature.

2.2. Photocatalytic and photoelectrochemical measurements

The photocatalytic activities were determined by the degradation of RhB aqueous solution under visible light irradiation in

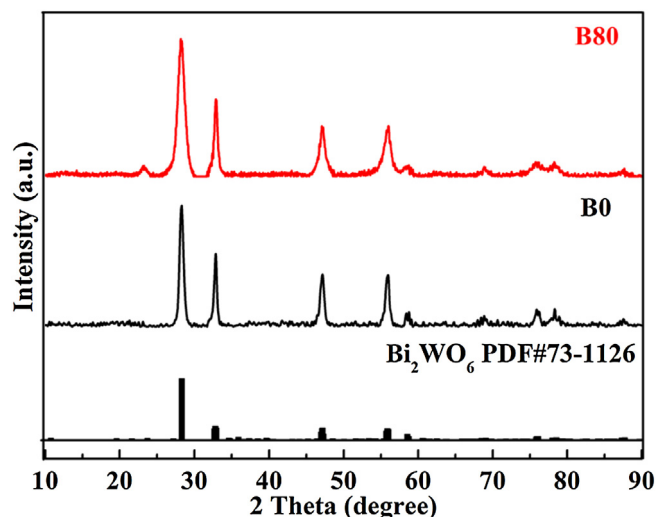


Fig. 1. XRD patterns of B0 and B80 samples.

quartz photochemical reactor. A 300 W Xenon lamp (Trusttech PLS-SXE 300, Beijing) covered with a UV filter ($\lambda > 400$ nm) was used as a light source. The photodegradation was performed at room temperature as follows: the RhB solution (10 mg L^{-1} , 100 mL) containing $0.05 \text{ g Bi}_2\text{WO}_6$ was carried out after 5 min ultrasonic process and kept in dark for 55 min to achieve adsorption–desorption equilibrium between dyes and photocatalysts under continuous magnetic stirring, then adding $0.1 \text{ mL H}_2\text{O}_2$ to reactor before irradiation. Every 10 min of time intervals, 3 mL mixture was collected from the suspension, followed by centrifuged at 10^4 rpm for 3 min. The absorbance of RhB solution was analyzed by measuring the absorbance at $\lambda = 554 \text{ nm}$ with the UV-vis spectrophotometer (PG, TU-1900).

The photoelectrochemical characteristics were measured in a CHI604C electrochemical working station using a standard three-compartment cell under visible light provided by a 300 W Xe lamp. The Bi_2WO_6 sample coated at FTO glass, a piece of Pt sheet, a Ag/AgCl electrode and 0.01 M sodium carbonate were used as the working electrode, the counter-electrode, the reference electrode and the electrolyte, respectively.

2.3. Gas sensor fabrication and measurement

The gas sensors were fabricated as follows: the as-prepared Bi_2WO_6 powder was mixed with the deionized water and coated onto an Al_2O_3 tube (4 mm in length, 1.2 mm in external diameter and 0.8 mm in internal diameter). The tubes were attached with a pair of gold electrodes to form a sensing film with thickness of $\sim 100 \mu\text{m}$. After drying 60 min at room temperature, the sensing devices were sintered at 400°C for 2 h. Then, the gas-sensing properties of the samples were determined under laboratory conditions. The response of the sensor was defined as $S = Ra/Rg$, where Ra and Rg were the resistances of the sensor in the air and target gas, respectively. The response and recovery times are defined as the time taken by the sensor to achieve 90% of the total resistance change during adsorption and desorption, respectively.

3. Results and discussion

The XRD patterns of as-prepared B0 and B80 samples (Fig. 1) show the similar diffraction characteristics and can be well-indexed as orthorhombic Bi_2WO_6 (JCPDS card No.73-1126), which implies the identical crystalline phase Bi_2WO_6 products are obtained and the excess WO_4^{2-} ions do not cause the phase change of Bi_2WO_6 .

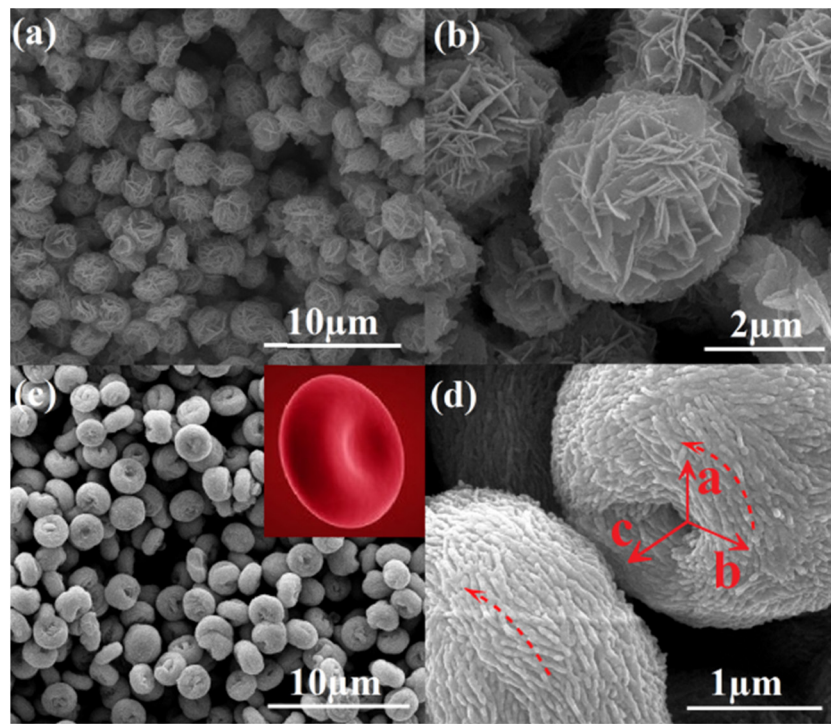


Fig. 2. FESEM images of B0 (a, b), B80 (c, d) and the photograph of erythrocyte (the insert of c).

In addition, the sharp and intense diffraction peaks indicate high crystallinity of the samples. The FESEM images of B0 and B80 samples are shown in Fig. 2. The typical Bi_2WO_6 microsphere with $\sim 3 \mu\text{m}$ diameter (B0) is obtained (as shown in Fig. 2a–b). When the W/Bi ratio is adjusted to 0.9, a unique Bi_2WO_6 hierarchical architecture with a size of $\sim 3 \mu\text{m}$ is achieved, which presents the superior monodispersity and uniformity. This architecture is similar to the morphology of erythrocyte (the photograph of erythrocyte is shown in the insert of Fig. 2c), so we denote it as erythrocyte-like Bi_2WO_6 . Noticeably, as shown in the high-magnification FESEM image of B80 (Fig. 2d), the erythrocyte-like hierarchical architecture is built by well-organized and directed self-assembly of abundant nano-blocks entwining along c axis at $a-b$ plane (as shown by red arrows). This building way results in the rugged and rough appearance as well as numerous mesoporous formation, which is further evidenced by the TEM and Barrett–Joyner–Halenda (BJH) pore diameter distribution analysis as follows.

Fig. 3a–b shows TEM images of individual erythrocyte-like architecture that is parallel and perpendicular to c axis, respectively. Fig. 3a displays an obvious brightness difference between the edge and center, as well as Fig. 3b displays a flat shape, further confirming erythrocyte-like morphology characteristic. The micro-structure of individual erythrocyte-like architecture is also observed by high-magnification TEM images in Fig. 3c and d. The image recorded at the edge of individual architecture (Fig. 3c) shows that it is actually built by 2D ultrathin nanoflakes with the thicknesses of $\sim 4.4 \text{ nm}$. In addition, these ultrathin nanoflakes exhibit well-organized assembly complying with a certain orientation, as marked by the red arrows in Fig. 3d. Moreover, the SAED is performed on the individual architecture (the insert of Fig. 3d). Unlike the polycrystalline diffraction rings, this diffraction rings are not closed completely. The periodic, symmetrical and alternate characteristic further reveals that ultrathin nanoflake units stack together to form 3D erythrocyte-like architecture with orientation assembly feature [28]. The lattice parameters of B80 sample are identified by HRTEM (Fig. 3e). The interplanar spacing of stacked

nanoflakes is 0.375 nm , which agrees well with the (111) planes of orthorhombic Bi_2WO_6 identically [29]. All above prove that the 3D erythrocyte-like Bi_2WO_6 hierarchical architecture assembled by ultrathin nanoflakes is successfully constructed using a facile anionic self-regulation strategy.

The formation mechanism of erythrocyte-like hierarchical architecture for B80 sample is investigated by the time-dependent experiment. Fig. S1 shows the FESEM and TEM images of morphology evolution for B80 sample with reaction time and its corresponding XRD patterns. When the reaction is carried out for 2 h, the low crystallinity Bi_2WO_6 precursor composed of nanoflakes is firstly formed according to FESEM and TEM images (Fig. S1a) as well as the corresponding widened XRD diffraction peaks (Fig. S1e). Proceeding reaction to 2.5 h, some erythrocyte-like Bi_2WO_6 hierarchical architectures are generated and coexist with nano-blocks composed of nanoflakes (Fig. S1b). As the reaction continues 3 h, more erythrocyte-like hierarchical architectures appear and the nano-blocks decrease (Fig. S1c). Further prolonging the reaction time to 3.5 h, the nano-blocks disappear and the evenly distributed and monodispersed erythrocyte-like architectures are achieved (Fig. S1d). The more and more narrow and sharpened of XRD diffraction peaks (Fig. S1e) imply that the crystallinity is gradually improved with reaction proceeding because of ripening and self-assembly process. The formation process of B80 sample reveals that the erythrocyte-like hierarchical architecture is assembled by secondary nano-blocks constructed by primary nanoflakes units.

Based on the above results, the possible crystal growth mechanism is shown in Scheme 1. It involves nucleation, oriented attachment and self-assembly process for construction of erythrocyte-like hierarchical architecture [30,31]. The orthorhombic Bi_2WO_6 is described schematically as a number of alternating $(\text{Bi}_2\text{O}_2)_n^{2+}$ and perovskite-like $(\text{WO}_4)_n^{2-}$ layers stacking at the vertical direction [32]. At the initial reaction stage, plenty of Bi_2WO_6 nanoflake crystal seeds are generated owing to the layered structure characteristic (nucleation process, Step 1). With the reaction proceeding, the excess WO_4^{2-} ions adsorb on the top and bottom surface of seeds and suppress their intrinsic

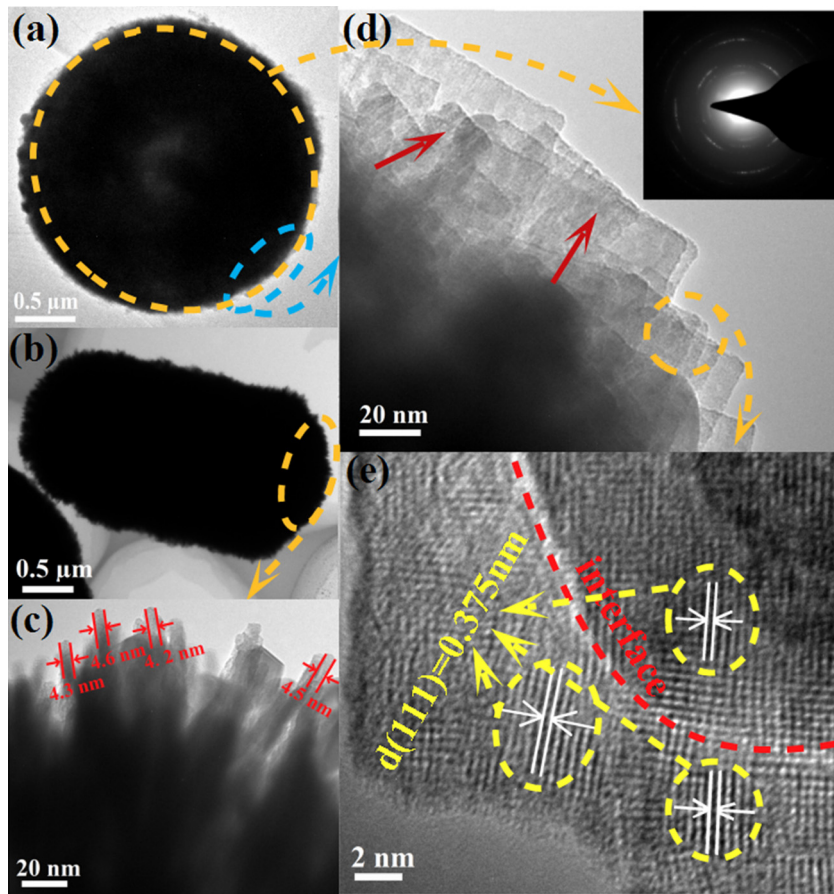
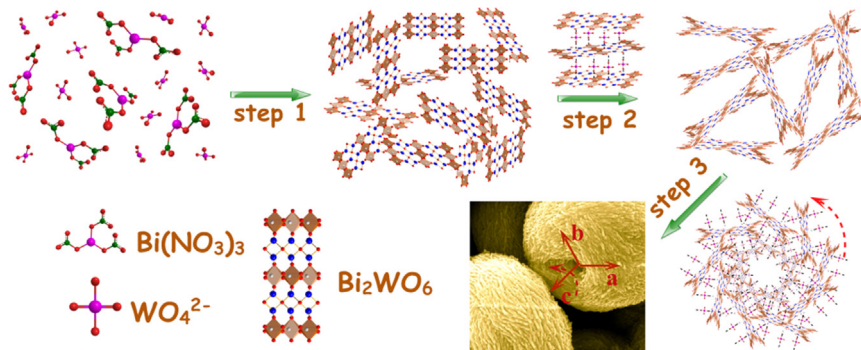


Fig. 3. TEM images of B80 sample (a–d), SAED pattern (the insert of d) recorded on individual erythrocyte-like microsphere and HRTEM image of the ultrathin nanoflake units (e).

anisotropic crystal growth, thus resulting in the generation of ultra-thin nanoflakes (growth process, Step 2). At the same time, some nanoflakes directionally overlap together with a certain orientation along the vertical direction through bridging and directing effects of WO_4^{2-} ions to form nano-blocks (oriented attachment process, Step 2). Finally, the excess WO_4^{2-} ions still adsorb on the nano-block surfaces accompanying with nanoflakes growing up and overlapping. It may produce larger space steric hindrance, which makes the nano-block units stack preferentially perpendicular to c axis and thus easily generate a curved nanostructure (self-assembly process, Step 3). At this step, the directing role of WO_4^{2-} absorbed on the nano-block surfaces may induce growth along horizontal and vertical directions. The growth rate of c axis is lower than the stacking velocity of perpendicular to the c axis in the nano-blocks

oriented self-assemble process due to the weaker adsorption force between WO_4^{2-} ions on the nano-blocks, which may be the non-equilibrium kinetic growth process [33]. Meanwhile, when the nano-block units stack rotundity, the further accumulation prefers to stack outward due to the internal space steric hindrance arising from adsorbed WO_4^{2-} ions. Thus, the erythrocyte-like Bi_2WO_6 hierarchical architecture is constructed through self-assembly and Ostwald ripening process in the subsequent step. It should be pointed out that the excess WO_4^{2-} ions are the dominant factor for the formation of erythrocyte-like Bi_2WO_6 hierarchical architecture. The adsorption effect of WO_4^{2-} ions on the B80 sample surface is evidenced by the following EDS and XPS analysis.

The chemical composition and surface states of B0 and B80 samples are investigated using the EDS and XPS technique. The EDS



Scheme 1. The schematic diagram of crystal growth mechanism for B80 sample.

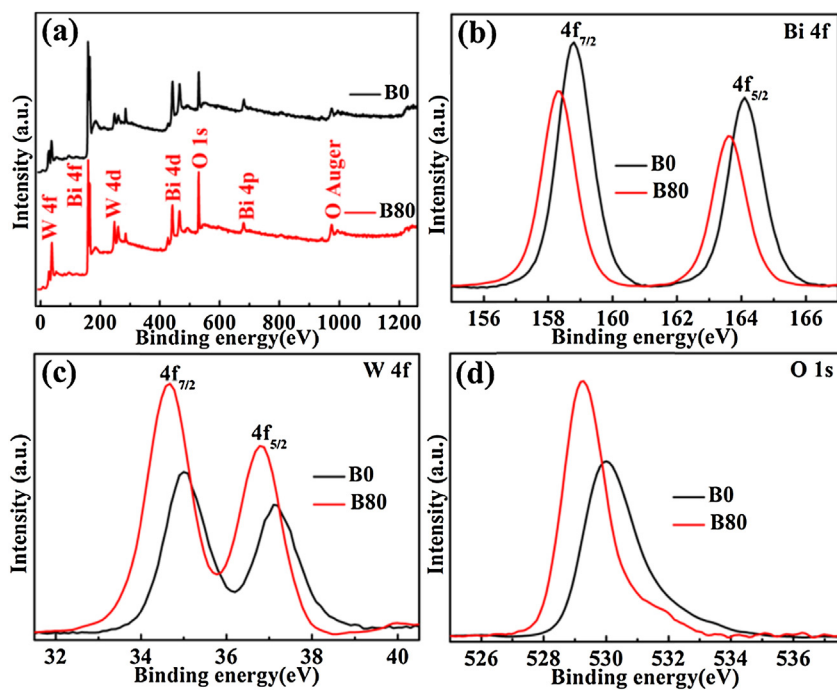


Fig. 4. Survey (a) and high-resolution XPS spectra of Bi 4f (b), W 4f (c) and O 1s (d) for B0 and B80 samples.

spectra in Fig. S2 exhibit that both B0 and B80 samples contain Bi, O and W elements. The relative content of W element in B80 sample is obvious higher than that in B0, which implies the excess WO_4^{2-} ions absorb on the B80 sample surface. The survey XPS spectra of B0 and B80 samples in Fig. 4a show the obvious binding energy peaks attributed to W 4f, Bi 4f, W 4d, Bi 4d, O 1s, Bi 4p and O auger state, respectively, which further indicates both of samples are composed of Bi, W, and O elements. The XPS spectra of B0 in Fig. 4b belong to the Bi^{3+} 4f_{7/2} and 4f_{5/2} states at 158.8 eV and 164.1 eV, respectively [34]. In addition, Fig. 4c exhibits the obvious binding energy peaks of B0 deriving from W^{6+} 4f_{7/2} (35.0 eV) and 4f_{5/2} (37.1 eV) states [35]. Furthermore, the binding energy peak in Fig. 4d at 530.0 eV agrees well with O 1s state in Bi_2WO_6 [36]. It is noteworthy that the binding energies of Bi 4f_{7/2}, W 4f_{7/2} and O 1s (158.3 eV, 34.7 eV and 529.2 eV) in B80 sample shift 0.5 eV, 0.3 eV and 0.8 eV toward low binding energy compared with that of B0, respectively. It has been reported that the increase/decrease in electron concentration can enhance/reduce the electron screening effect, leading to weakening/strengthening the binding energy [37,38]. Therefore, the shifting to lower binding energy of O, Bi and W elements in XPS spectra of B80 sample results from the increased electron concentration caused by WO_4^{2-} ions adsorbing on the surface, which is further evidenced by the higher surficial element contents of W and O in B80 than that in B0 sample (Table S1).

The UV-vis DRS spectra of B0 and B80 are measured to evaluate light absorption property of the samples (Fig. 5). The steep shapes indicate that the intense absorptions are not due to the transition from the impurity level but band-gap transition [39]. It is crucial that the light absorption ability of B80 is significantly enhanced and its absorption edge is redshifted compared with that of B0. The band gaps of B0 and B80 are further estimated according to the research method of crystal semiconductor reported by M.A. Butler (See supporting information) [40]. Bi_2WO_6 is a typical indirect band gap semiconductor [41]. Using plots of $(\alpha h\nu)^{1/2}$ versus $h\nu$ (the insert of Fig. 5), we achieve band gap values of 2.71 eV and 2.75 eV for B80 and B0 samples, respectively. It implies electrons are more easily excited from the VB to CB for B80 sample [2]. In addition, VB and CB positions are calculated via employing empirical formula (See

Table S2). The VB top and CB bottom of B80 are estimated to be 3.05 eV and 0.34 eV, which are similar to that of B0 (3.07 eV and 0.32 eV). It indirectly suggests the effects of redox ability of the B80 sample on improving activity are insignificant.

The photocatalytic activities of as-prepared samples are evaluated by degradation of RhB solution under visible light. The dynamic curves of photodegradation in Fig. 6a show the photolysis of RhB is negligible without photocatalyst and the photocatalytic activities of B0 and B80 are obvious higher than that of P25. Importantly, RhB is completely removed within 15 min over the B80 sample, which is far faster than that of B0 (35 min). Furthermore, the kinetic curves of RhB photodegradation can be approximated as a pseudo-first-order process [42] and the plots of $\ln(C_0/C)$ versus time are performed (Fig. 6b). The removal rate constant k of RhB photodegradation over B80 is 0.212 min^{-1} , which reaches to 2.62, 16.3 and 70.7 times as much as that of B0 (0.081 min^{-1}), P25 (0.013 min^{-1}) and blank (0.003 min^{-1}), respectively. In addition, the photocatalysis activity of B80 is still higher than that of B0 without adding H_2O_2 (Fig. S3). Fig. 6c describes

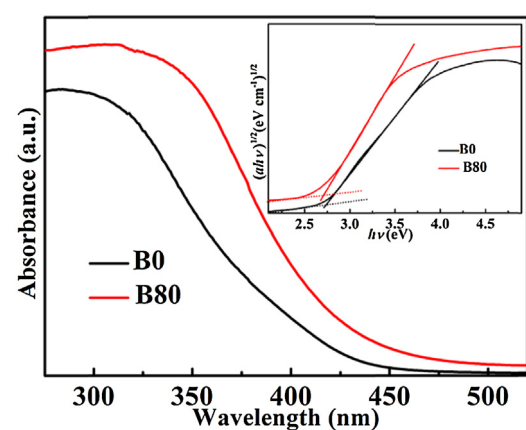


Fig. 5. UV-vis DRS and plots of $(\alpha h\nu)^{1/2}$ versus $h\nu$ (the insert) of B0 and B80 samples.

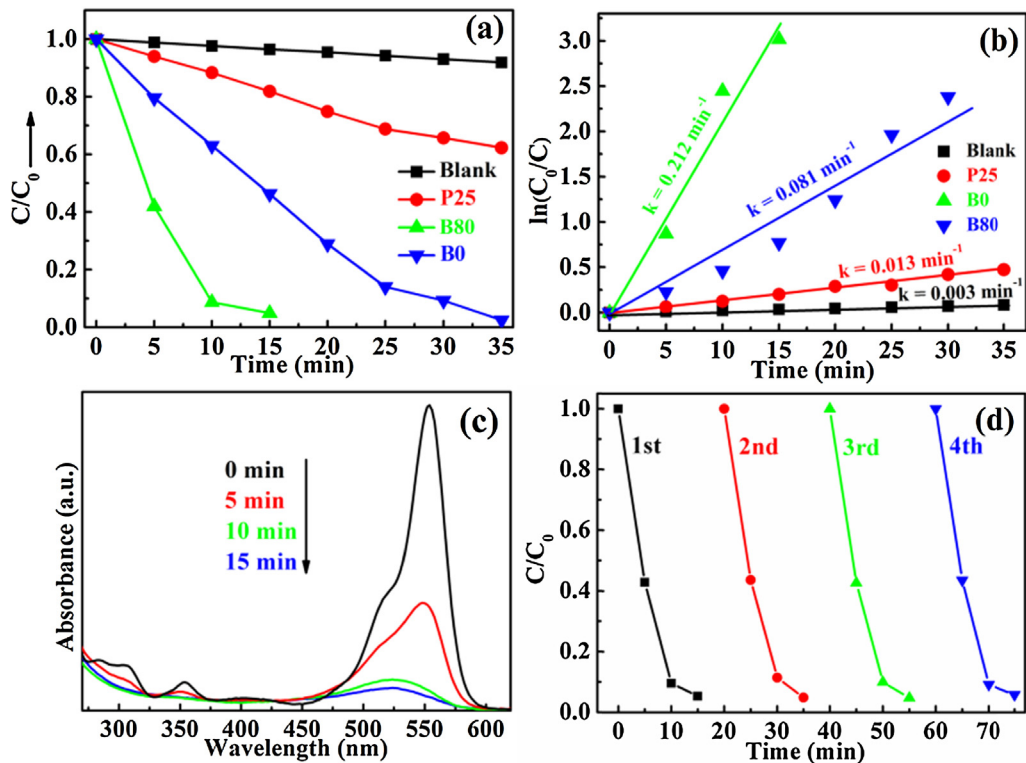


Fig. 6. Dynamic curves of photodegradation (a), plots of $\ln(C_0/C)$ versus time and rate constant k (b) for RhB solutions over different samples, absorption spectra variations (c) and cycle runs (d) of RhB solutions over B80 sample.

the absorbance variation of RhB solutions over the B80 sample during photodegradation process. It is notable that the absorbance of RhB solution at ultraviolet region of 270–400 nm besides visible region almost disappears after 15 min. The results indirectly prove the conjugated chromophore structure may be destroyed and the organic dye molecules are completely decomposed into small organic/inorganic molecules or/and ions products [2]. Taking into account the stability and reusability of photocatalyst, the cycle degradation experiments of RhB solutions are carried out (Fig. 6d), the photocatalytic activity of B80 sample in which is not significant loss after four cycles. The above results indicate that the as-achieved erythrocyte-like Bi_2WO_6 hierarchical architecture shows high photocatalytic activity, stability and durability.

Moreover, it can be expected that such a unique erythrocyte-like Bi_2WO_6 hierarchical architecture may be a potential candidate

for gas-sensing materials. Two sensors are fabricated from B80 and B0 samples and their gas-sensing properties for ethanol and acetone gas in dry air are researched at different temperature (Fig. 7a). Two sensors show that the different maximal response values of 39.82 and 16.21 to ethanol and acetone gas are obtained at 275 °C and 300 °C, which is 8.52 and 19.0 times than that of B0, respectively. Importantly, the gas response values of B80 sensor to ethanol and acetone gas are far higher than that of B0 at 250–350 °C. The more sensitive response to ethanol than that of acetone gas may result from that the former has more intense reduction property that is easily reduced by the strong oxidizing species adsorbed on the Bi_2WO_6 surface [27]. Meanwhile, the response–recovery curves of B80 sensor to ethanol with different gas concentrations at 275 °C are shown in Fig. 7b, it is apparently observed that the response–recovery time increases with

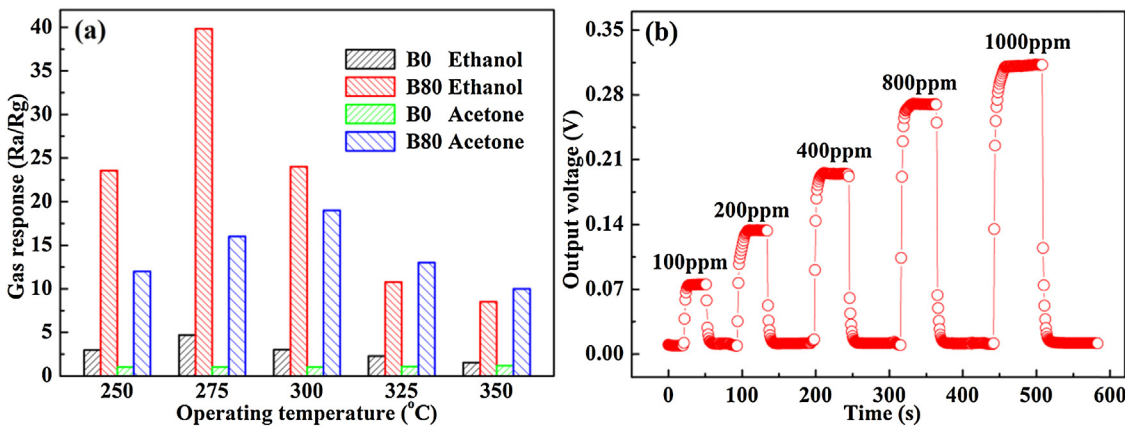


Fig. 7. (a) Temperature dependence of gas response for sensors fabricated by B0 and B80 (the gas concentration is 1000 ppm); (b) the operating temperature change and their highest response to response-recovery curve of B80 sensor at different ethanol gas concentrations ($T=275$ °C).

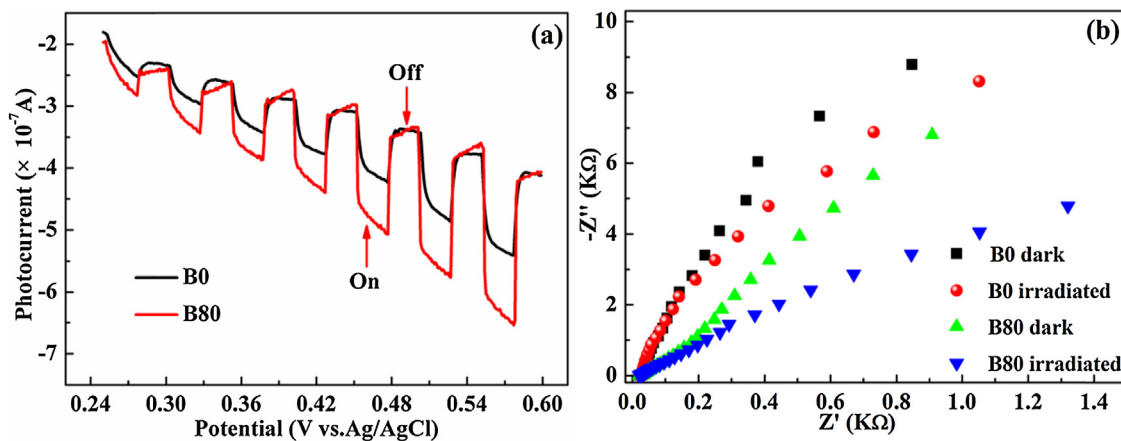


Fig. 8. Photocurrent responses (a) and EIS plots (b) of B0 and B80 samples.

increasing ethanol concentration and a wide detection range from 100 to 1000 ppm.

The photocatalytic activity and gas-sensing property are closely concerned with the electron transport behavior. The intense photocurrent suggests the high charge collection efficiency on the electrode surface, and indirectly evidences the high separated efficiency of electron–hole pairs [43,44]. The B80 electrode exhibits the greater photocurrent response than that of B0 electrode under visible light (Fig. 8a), which demonstrates that the former can separate electron–hole pairs more effectively. Furthermore, the electrochemical impedance spectroscopies (EIS) in Fig. 8b show that the arc radius of EIS Nyquist plots for B80 electrode under the dark and visible light are both smaller than that of B0 electrode. It implies the faster interfacial charge transfer in B80 electrode [45]. Additionally, it is reported that photoluminescence (PL) emission is mainly caused by the recombination of electron–hole pairs [46]. Fig. 9 shows that the PL emission peaks of two samples locate at 400 nm, which ascribes to the transfer of band gap. The lower PL intensity of B80 sample indicates the recombination of charge carriers is greatly inhibited. The photoelectrochemical and photoluminescent characteristics reveal the erythrocyte-like Bi_2WO_6 hierarchical architecture has lower recombination probability and faster transport velocity than the typical Bi_2WO_6 microsphere. As a photocatalyst, the erythrocyte-like Bi_2WO_6 hierarchical architecture improves photocatalytic activity through enhancing the transfer and separation efficiency of electrons–hole pairs. As a gas-sensing material, the faster transfer velocity of carriers can immediately reduce adsorbed O_2 molecules into more O^- activated

species, leading to shortening response time and improving sensitivity of sensor.

Furthermore, the specific surface area and pore diameter distribution are also the important parameters for photocatalytic activity and gas-sensing property. Nitrogen adsorption and desorption measurements and Barrett–Joyner–Halenda (BJH) pore diameter distribution are further carried out (Fig. 10a). According to the IUPAC classifications, the isotherm of B0 sample is categorized as type II with a H3 hysteresis loop, which indicates the presence of macropores ($>50 \text{ nm}$) [47,48] in line with the corresponding pore diameter distribution (the insert of Fig. 10a). Significantly, the isotherm of B80 sample in Fig. 10b can be categorized as type IV according to a hysteresis loop appeared in the range of 0.4–1.0 (P/P_0), which indicates the presence of mesopores (2–50 nm) [20]. Meanwhile, the hysteresis loop almost approaching 1 (P/P_0) also suggests the presence of macropores. It is also confirmed by the corresponding pore diameter distributions (inset in Fig. 10b), which shows two peaks of mesoporous along with macropores up to 200 nm. In addition, the Brunauer–Emmett–Teller (BET) surface area of B80 sample ($41.80 \text{ m}^2 \text{ g}^{-1}$) is larger than that of B0 ($25.02 \text{ m}^2 \text{ g}^{-1}$). So the B80 sample has a larger specific surface area and more abundant pore distribution than the typical Bi_2WO_6 microsphere. It provides a mass of reactive active sites and molecular transport channels, thus enhancing the photocatalytic activity and gas-sensing property materials.

Scheme 2 illustrates the possible photocatalytic (a) and gas-sensing (b) mechanism schematics. As can be seen in **Scheme 2a**, when the B80 sample serves as photocatalyst, plenty of electrons–hole pairs generate under the visible light irradiation, then separate and transfer to the sample surface. A little part of electrons are captured by the dissolved oxygen in the water to produce superoxide radicals $\cdot\text{O}_2^-$ degrading RhB molecules [49,50]. In addition, most of electrons react with H_2O_2 molecules in the water to yield abundant hydroxyl radicals $\cdot\text{OH}$ to remove RhB molecules. Meanwhile, the holes can also directly degrade RhB molecules [51,52]. It should be pointed out that H_2O_2 serves as an efficient electron scavenger, which can also facilitate separation and transfer of charge carriers to improve the photocatalytic activity. By contrast, the gas-sensing mechanism is different from photocatalytic mechanism (**Scheme 2b**). When the fabricated sensor is exposed to air, O_2 molecules adsorbed on the B80 sample surface capture electrons on CB and transform into O^- species at a certain temperature [23,24]. It results in forming a space-charge layer, which increases the potential barrier, and thus a higher resistance. When the sensor is exposed to ethanol or acetone atmosphere, adsorbed O^- species on the Bi_2WO_6 surface can oxidize ethanol or acetone to CO_2 and H_2O , as well as release electrons into the CB of B80 sample

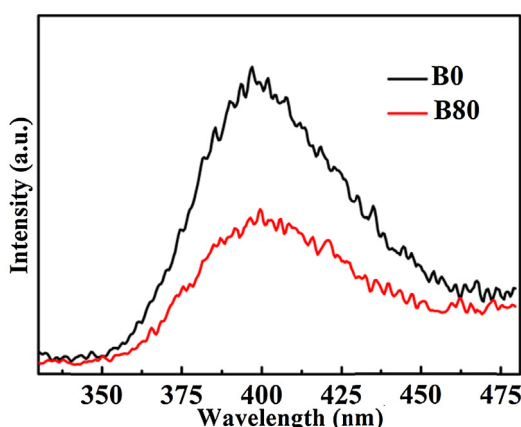


Fig. 9. PL spectra of B0 and B80 samples.

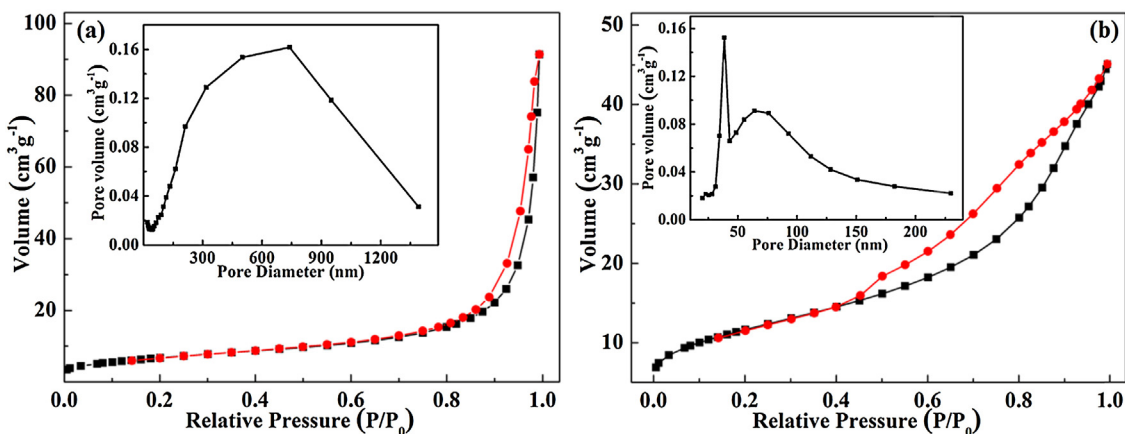
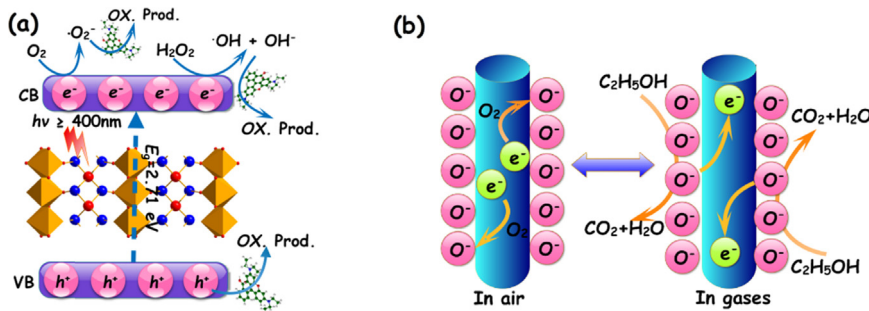


Fig. 10. N₂ adsorption–desorption curves and pore diameter distributions (insert) of B0 (a) and B80 (b) samples.



Scheme 2. Possible photocatalytic (a) and gas-sensing mechanism (b).

again. This result can increase the carrier concentration of B80, thus reducing resistance of the sensor.

4. Conclusions

In summary, using a facile anionic self-regulation strategy, a 3D erythrocyte-like Bi₂WO₆ hierarchical architecture is firstly constructed via a facile hydrothermal process without any additives. The novel hierarchical architecture is assembled by unique ultra-thin nanoflakes with the thickness of ~4.4 nm. It not only displays high specific surface area and abundant mesoporous distribution but also facilitates transfer and separation of charge carriers. As a result, it markedly improves the photocatalytic activity and gas-sensing property relative to the typical Bi₂WO₆ microsphere. This work provides a promising route to design other ideal Bi-based oxide hierarchical architectures for future applications.

Acknowledgments

This work was financially supported by the National Natural Science Foundation of China (21271055) and Province Natural Science Foundation of Heilongjiang Province (ZD201011). We acknowledge for the support by Fundamental Research Funds for the Central Universities (HIT. IBRSEM. A. 201410), Open Project of State Key Laboratory of Urban Water Resource and Environment, Harbin Institute of Technology (No. QAK201304) and Program for Innovation Research of Science in Harbin Institute of Technology (PIRS of HIT B201412).

Appendix A. Supplementary data

Supplementary data associated with this article can be found, in the online version, at <http://dx.doi.org/10.1016/j.apcatb.2014.07.060>.

References

- [1] Y.F. Li, Z.P. Liu, J. Am. Chem. Soc. 133 (2011) 15743–15752.
- [2] H.J. Dong, G. Chen, J.X. Sun, C.M. Li, Y.G. Yu, D.H. Chen, Appl. Catal. B: Environ. 134–135 (2013) 46–54.
- [3] M. Wu, X. Lin, Y. Wang, L. Wang, W. Guo, D. Qi, X. Peng, A. Hagfeldt, M. Grätzel, T. Ma, J. Am. Chem. Soc. 134 (2012) 3419–3428.
- [4] J.X. Sun, G. Chen, J.Z. Wu, H.J. Dong, G.H. Xiong, Appl. Catal. B: Environ. 132–133 (2013) 304–314.
- [5] W. Hong, Y. Chen, X. Feng, Y. Yan, X.B. Hu, B.Y. Zhao, F. Zhang, D. Zhang, Z. Xu, Y. Lai, Chem. Commun. 49 (2013) 8229–8231.
- [6] S. Agarwala, Z.H. Lim, E. Nicholson, G.W. Ho, Nanoscale 4 (2012) 194–205.
- [7] Z. Zanolli, R. Leghrif, A. Felten, J.J. Pireaux, E. Llobet, J.C. Charlier, ACS Nano. 5 (2011) 4592–4599.
- [8] A. Devadoss, P. Sudhagar, S. Das, S.Y. Lee, C. Terashima, K. Nakata, A. Fujishima, W. Choi, Y.S. Kang, U. Paik, ACS Appl. Mater. Interfaces 6 (2014) 4864–4871.
- [9] J.X. Zhu, Z.Y. Yin, D. Yang, T. Sun, H. Yu, H.E. Hoster, H.H. Hng, H. Zhang, Q.Y. Yan, Energy Environ. Sci. 6 (2013) 987–993.
- [10] X.J. Wei, W. Wang, K.Z. Che, J. Phys. Chem. C 117 (2013) 23716–23729.
- [11] S.Y. Dong, J.L. Feng, Y.K. Li, L.M. Hu, M.L. Liu, Y.F. Wang, Y.Q. Pi, J.Y. Sun, J.H. Sun, Appl. Catal. B: Environ. 152–153 (2014) 413–424.
- [12] J.Y. Liao, B.X. Lei, D.B. Kuang, C.Y. Su, Energy Environ. Sci. 4 (2011) 4079–4085.
- [13] Y.H. Choi, D.H. Kim, H.S. Han, S. Shin, S.H. Hong, K.S. Hong, Langmuir 30 (2014) 700–709.
- [14] L.W. Zhang, Y.J. Wang, H.Y. Cheng, W.Q. Yao, Y.F. Zhu, Adv. Mater. 21 (2009) 1286–1290.
- [15] L.S. Zhang, H.L. Wang, Z.G. Chen, P.K. Wong, J.S. Liu, Appl. Catal. B: Environ. 106 (2011) 1–13.
- [16] A.K.P. Mann, S.E. Skrabalak, Chem. Mater. 23 (2011) 1017–1022.
- [17] D.K. Ma, S.M. Huang, W.X. Chen, S.W. Hu, F.F. Shi, K.L. Fan, J. Phys. Chem. C 113 (2009) 4369–4374.
- [18] D.B. Kuang, T. Brezesinski, B. Smarsly, J. Am. Chem. Soc. 126 (2004) 10534–10535.
- [19] Z.Q. Li, Y. Ding, Y.J. Xiong, Y. Xie, Chem. Commun. 7 (2005) 918–920.
- [20] Y.Y. Li, J.P. Liu, X.T. Huang, G.Y. Li, Cryst. Growth Des. 7 (2007) 1350–1355.
- [21] Y. Tian, G.M. Hua, N. Li, M. Fang, L.D. Zhang, J. Alloys Compd. 509 (2011) 724–730.
- [22] J. Wu, F. Duan, Y. Zheng, Y. Xie, J. Phys. Chem. C 111 (2007) 12866–12871.
- [23] L.S. Zhang, W.Z. Wang, L. Zhou, H.L. Xu, Small 3 (2007) 1618–1625.
- [24] M. Shang, W.Z. Wang, H.L. Xu, Cryst. Growth Des. 9 (2009) 991–996.
- [25] D.Q. He, L.L. Wang, H.Y. Li, T.Y. Yan, D.J. Wang, T.F. Xie, Cryst. Eng. Comm. 13 (2011) 4053–4059.
- [26] Z. Lou, J.N. Deng, L.L. Wang, L.J. Wang, T. Zhang, Sens. Actuators B-Chem. 182 (2013) 217–222.

- [27] D.J. Wang, Y.Z. Zhen, G.L. Xue, F. Fu, X.M. Liu, D.S. Li, *J. Mater. Chem. C* 1 (2013) 4153–4162.
- [28] Z.H. Ibupoto, K. Khun, V. Beni, X. Liu, M. Willander, *J. Am. Chem. Soc.* 126 (2004) 8124–8125.
- [29] L. Ge, J. Liu, *Appl. Catal. B: Environ.* 105 (2011) 289–297.
- [30] Q. Zhang, S.J. Liu, S.H. Yu, *J. Mater. Chem.* 19 (2009) 191–207.
- [31] R.H. Ouyang, J.X. Liu, W.X. Li, *J. Am. Chem. Soc.* 135 (2013) 1760–1771.
- [32] C. Zhang, Y. Zhu, *Chem. Mater.* 17 (2005) 3537–3545.
- [33] Y.S. Luo, X.J. Dai, W.D. Zhang, Y. Yang, C.Q. Sun, S.Y. Fu, *Dalton Trans.* 39 (2010) 2226–2231.
- [34] D.J. Wang, G.L. Xue, Y.Z. Zhen, F. Fu, D.S. Li, *J. Mater. Chem.* 22 (2012) 4751–4758.
- [35] J.H. Ryu, S.Y. Bang, W.S. Kim, G.S. Park, K.M. Kim, J.W. Yoon, K.B. Shim, N. Koshizaki, *J. Alloys Compd.* 441 (2007) 146–151.
- [36] J. Ren, W.Z. Wang, S.M. Sun, L. Zhang, J. Chang, *Appl. Catal. B: Environ.* 92 (2009) 50–55.
- [37] Z.Y. Zhang, C.L. Shao, X.H. Li, Y.Y. Sun, M.Y. Zhang, J.B. Mu, P. Zhang, Z.C. Guo, Y.C. Liu, *Nanoscale* 5 (2013) 606–618.
- [38] X.H. Li, H.Y. Xu, X.T. Zhang, Y.C. Liu, J.W. Sun, Y.M. Lu, *Appl. Phys. Lett.* 95 (2009) 191903.
- [39] A. Kudo, I. Tsuji, H. Kato, *Chem. Commun.* (2002) 1958–1959.
- [40] G.B. Hoflund, J.F. Weaver, W.S. Epling, *Surf. Sci. Spectra* 3 (1994) 157–162.
- [41] J.W. Tang, Z.G. Zou, J.H. Ye, *J. Phys. Chem. C* 111 (2007) 12779–12785.
- [42] I.K. Konstantinou, T.A. Albanis, *Appl. Catal. B: Environ.* 49 (2004) 1–14.
- [43] H.J. Dong, G. Chen, J.X. Sun, Y.J. Feng, C.M. Li, G.H. Xiong, C.D. Lv, *Dalton Trans.* 43 (2014) 7282–7289.
- [44] Y.H. Ng, I.V. Lightcap, K. Goodwin, M. Matsumura, P.V. Kamat, *J. Phys. Chem. Lett.* 1 (2010) 2222–2227.
- [45] W.H. Leng, Z. Zhang, J.Q. Zhang, C.N. Cao, *J. Phys. Chem. B* 109 (2005) 15008–15023.
- [46] J.Z. Ma, H.M. Wu, Y.C. Liu, H. He, *J. Phys. Chem. C* 118 (2014) 7434–7441.
- [47] G.I.N. Waterhouse, G.A. Bowmaker, J.B. Metson, *Phys. Chem. Chem. Phys.* 3 (2001) 3838–3845.
- [48] X.F. Wang, S.F. Li, H.G. Yu, J.G. Yu, *J. Mol. Catal. A: Chem.* 334 (2011) 52–59.
- [49] Z.K. Cui, D.W. Zeng, T.T. Tang, J. Liu, C.S. Xie, *Catal. Commun.* 11 (2010) 1054–1057.
- [50] Y.M. Xu, C.H. Langfor, *Langmuir* 17 (2001) 897–902.
- [51] C.M. Li, G. Chen, J.X. Sun, H.J. Dong, Y. Wang, C.D. Lv, *Appl. Catal. B: Environ.* 160–161 (2014) 383–389.
- [52] Y. Xie, G. Ali, S.H. Yoo, S.O. Cho, *ACS Appl. Mater. Interfaces* 2 (2010) 2910–2914.